Open Research Online

The Open University's repository of research publications
and other research outputs

Unveiling cloudy exoplanets: the influence of cloud model choices on retrieval solutions

Journal Item

oro.open.ac.uk

Unveiling cloudy exoplanets: the influence of cloud model choices on retrieval solutions

Joanna K. Barstow ®[1,2]★

[1] *School of Physical Sciences, The Open University, Walton Hall, Milton Keynes MK7 6AA, UK*
[2] *Department of Physics and Astronomy, University College London, Gower Street, London WC1E 6BT, UK*

ABSTRACT

In recent years, it has become clear that a substantial fraction of transiting exoplanets have some form of aerosol present in their atmospheres. Transit spectroscopy – mostly of hot Jupiters, but also of some smaller planets – has provided evidence for this, in the form of steep downward slopes from blue to red in the optical part of the spectrum, and muted gas absorption features throughout. Retrieval studies seeking to constrain the composition of exoplanet atmospheres must therefore account for the presence of aerosols. However, clouds and hazes are complex physical phenomena, and the transit spectra that are currently available allow us to constrain only some of their properties. Therefore, representation of aerosols in retrieval models requires that they are described by only a few parameters, and this has been done in a variety of ways within the literature. Here, I investigate a range of parametrizations for exoplanet aerosol and their effects on retrievals from transmission spectra of hot Jupiters HD 189733b and HD 209458b. I find that results qualitatively agree for the cloud/haze itself regardless of the parametrization used, and indeed using multiple approaches provides a more holistic picture; the retrieved abundance of H_2O is also very robust to assumptions about aerosols. I also find strong evidence that aerosol on HD 209458b covers less than half of the terminator region, whilst the picture is less clear for HD 189733b.

Key words: radiative transfer – techniques: spectroscopic – planets and satellites: atmospheres.

1 INTRODUCTION

In recent years, the characterization of transiting exoplanet atmospheres has evolved to the extent that several comparative studies of the most favourable targets have been published. These targets mostly consist of hot Jupiters, which are ideal candidates for transit spectroscopy. Their high temperatures and H_2–He-dominated atmospheres result in large atmospheric scale heights, and therefore large fluctuations in the transit depth as a function of wavelength.

Evidence for the presence of cloud or haze (or a lack of evidence for its absence) has been found in the majority of hot Jupiter spectra. Whilst simulations including condensational processes or cloud microphysics can predict the cloud that is expected to form under particular circumstances, we have no prior knowledge of likely cloud structures on intensely irradiated, hot worlds. Therefore, simple, parametrized retrieval models (e.g. Madhusudhan & Seager 2009; Lee, Fletcher & Irwin 2012; Line et al. 2013; Benneke 2015; Waldmann et al. 2015; Blecic, Dobbs-Dixon & Greene 2017; Cubillos et al. 2017; Mai & Line 2019; Kitzmann et al. 2020; Mollière et al. 2020) are a crucial part of a data-driven approach to learning about exoplanet aerosols.

Cloud refers to aerosol produced via condensation, whereas haze is aerosol that is photochemically produced (see e.g. Hörst 2017). We do not yet know which mechanism is responsible for aerosol production on exoplanets, but in general discussion about likely constituents centres around condensates (e.g. Helling et al. 2016; Wakeford et al.

2017; the former elaborates on the full complexity of the process and the need for seed particles). Given the emphasis on condensation, in this work I will refer to exoplanet aerosols as cloud, as is commonly done in the literature.

Four comparative retrieval studies have been recently published, two dealing with data from the *Hubble Space Telescope* (*HST*) Wide Field Camera 3 (WFC3) instrument only (Fisher & Heng 2018; Tsiaras et al. 2018), and two also incorporating *HST* Space Telescope Imaging Spectrograph (STIS) and *Spitzer* Infrared Array Camera (IRAC) data (Barstow et al. 2017; Pinhas et al. 2019). The general philosophy of these studies is the same; to use a relatively agnostic model set-up to retrieve the basic atmospheric properties for a range of planets, in such a way that the results are directly comparable. Retrieved properties common to all studies include H_2O abundance, temperature structure (with varying assumptions), radius or pressure baseline, and cloud parameters. A detailed comparison of the retrieval results from these studies is included in Barstow & Heng (2020). Of particular interest in this work are the differences in cloud parametrization, and the effects of this on the retrieved cloud properties.

In this work, I contrast the different approaches to parametrizing cloud, and test each of the cloud models in turn on a benchmark data set. For this purpose, I have chosen the spectra of HD 189733b (Bouchy et al. 2005) and HD 209458b (Charbonneau et al. 2000) as presented in Sing et al. (2016). These are the most precisely measured hot Jupiter spectra so far, and both contain clear evidence for scattering particles in the atmosphere of the planet, albeit of different kinds. Whilst the HD 189733b spectrum has a substantial slope in the visible, which may be an indicator of the presence

★ E-mail: jo.barstow@open.ac.uk

of small, Rayleigh scattering particles, the HD 209458b spectrum has a muted H_2O feature but very little optical slope, suggesting its spectrum is more likely to be dominated by larger particles. Together, these spectra provide a good test of the ability of each cloud model to match a diverse range of observations.

Previous work by Mai & Line (2019) applies a similar approach, for more physically motivated cloud parametrizations, to simulated *James Webb Space Telescope* (*JWST*) spectra of WASP-62b. They conclude that including cloud in the model is necessary for retrieving spectra of a cloudy planet, but that all cloud models they tested provide unbiased solutions for other atmospheric properties, despite the differences in approach.

In Sections 2.1 and 2.2, I describe the basic retrieval model set-up. In Section 2.3, I discuss the differences between the cloud models used in each paper, and the way in which they have been implemented. Retrieval results are presented in Section 3, and discussed further in Section 4.

2 RETRIEVAL MODEL SET-UP

2.1 NEMESIS

I use the NEMESIS radiative transfer and retrieval code, originally developed for Solar system planets (Irwin et al. 2008) and subsequently extended for use with exoplanets (Lee et al. 2012; Barstow et al. 2017; Krissansen-Totton et al. 2018). NEMESIS incorporates a fast, 1D radiative transfer calculation, which makes use of the correlated k approximation allowing absorption line data to be stored in a quick look up table (Lacis & Oinas 1991). Whilst originally NEMESIS used an optimal estimation technique to converge on the most likely atmospheric solution (Rodgers 2000), the dependence of this method on an informative prior means that it is less appropriate for exoplanets since in this case our prior knowledge is severely restricted. Instead, a recent upgrade (Krissansen-Totton et al. 2018) sees NEMESIS interface with the PYMULTINEST algorithm (Feroz & Hobson 2008; Feroz, Hobson & Bridges 2009; Buchner et al. 2014; Feroz et al. 2019).

2.2 Basic atmospheric retrieval model

The basic atmospheric models for HD 189733b and HD 209458b are based on those used in Barstow et al. (2017). We restrict the spectrally active gases to Na, K, and H_2O, as these are the only gases for which strong evidence has been found, with prior ranges for $\log$ (Na, K) of -13 to -3, and for $\log (H_2O)$ of -8 to -2. They are assumed to be well mixed, so gas abundances account for three parameters in the retrieval. The bulk of the atmosphere is a mixture of H_2 and He.

Line data for H_2O are taken from the BT2 data base (Barber et al. 2006), and those for Na and K are from the Vienna Atomic Line Database (VALD; Heiter et al. 2008). Collision-induced absorption for H_2 and He is taken from Borysow & Frommhold (1989, 1990), Borysow, Frommhold & Moraldi (1989), Borysow, Jorgensen & Fu (2001), and Borysow (2002). The Na and K features are expected to be strongly pressure broadened in the wings of the absorption lines. To account for this, the line wing cut-off for Na and K is extended to 6000 cm^{-1} from the line centre, as opposed to the more usual 25 cm^{-1}. Welbanks et al. (2019) explore the H_2-broadened shape of these lines further, and find that at temperatures of 2000 K the wings of both Na and K features do not extend beyond 1.4 μm; cutting at 6000 cm^{-1} for the K band means the line extends to 1.41 μm. In any case, for cloudy planets the pressure-broadened line wings are generally obscured by the cloud, which can be seen to be the case here.

The temperature profile is represented as an isotherm for $P <$ 0.1 atm and $P > 1.0$ atm, and as an adiabat in between. The stratospheric temperature T_{strat} (prior range: 100–3000 K) is therefore the single temperature variable in the model. I also retrieve the planetary radius at the 10 atm pressure level, because the literature value for this is taken from the white light transit, and the pressure that this refers to is extremely dependent on the atmospheric properties of the planet. For further context as to why this is necessary, see Barstow & Heng (2020, section 1.2 and references therein). The prior range for this value is planet specific, from 0.9 to 1.3 R_J for HD 189337b, and from 1.1 to 1.5 R_J for HD 209458b. Therefore, before cloud is introduced, the model atmosphere contains five free parameters.

2.3 Cloud models

Cloud formation is a complex process, and reducing clouds to something that can be represented by a minimal number of parameters is challenging. As a result, different teams have adopted a variety of approaches, but all have some factors in common.

The key features of a cloud that are important to capture when modelling transit spectra are (1) the pressure level at which the cloud becomes opaque and (2) the wavelength dependence of this. These effects can be represented in a variety of ways. Additional effects may also be important under certain circumstances; if a cloud layer is optically thin, the location of the cloud base may also become important. For hot Jupiters, which are tidally locked, strong winds are thought to result in the temperature varying considerably between the morning and evening terminators, which in turn could lead to variation in cloud coverage (e.g. Line & Parmentier 2016); it may therefore also be necessary to include some formulation for fractional cloud cover around the terminator. The approaches to representing these key cloud features vary between the four comparative studies, and are summarized below.

Barstow et al. (2017, hereafter B17) use a grid of cloud models. They assume that the cloud has uniform specific density for pressures above a variable cloud top pressure. The cloud is treated either as Rayleigh scattering (scattering efficiency scales as $1/\lambda^4$, representing small particles) or grey (constant scattering efficiency). Two vertical cloud distributions are tested – the cloud either extends from the top pressure to the bottom of the atmosphere, or extends downwards by a decade in pressure. The second approach allows a detached haze layer to be simulated and a deep cloud deck. Finally, total optical depth is a free parameter in an optimal estimation retrieval for each cloud model.

In this work, the B17 model has been extended from the grid-search approach to include four free parameters: total nadir optical depth τ; top pressure P_{top}; base pressure P_{base}; and scattering index γ, where the wavelength dependence of the extinction efficiency is proportional to $\lambda^{-\gamma}$.

Tsiaras et al. (2018, hereafter T18) and Fisher & Heng (2018, hereafter F18) use effectively the same cloud model as each other, based on that presented by Kitzmann & Heng (2018), which in turn evolved from models used by Lee, Heng & Irwin (2013) and Lavie et al. (2017). They use an analytical model to capture the functional dependence of cloud extinction on wavelength. As described in F18, the cloud opacity is parametrized as follows:

$$\kappa_{\text{cloud}} = \frac{\kappa_0}{Q_0 x^{-a} + x^{0.2}}, \tag{1}$$

where κ_0 is an optical depth scaling factor, Q_0 determines the wavelength at which the extinction efficiency peaks, a is a scattering

Table 1. Variable cloud parameters grouped by type, for each of the models considered. Quantities are as defined in the text. Prior ranges as used in the retrieval are also included.

Property	B17 (updated)	T18	F18	P19
Opacity	τ	χ_c	κ_0	a
	$10^{-10}, 10^{20}$	$10^{-10}, 10^{13}$	$10^{-10}, 10^{13}$	$10^{-10}, 10^{20}$
Scat index	$-\gamma$	-4	$-a$	$-\gamma$
	$0, 14$	Fixed	$3, 7$	$0, 14$
Top pressure	$P_{top, all}$	$P_{top, grey}$	None	$P_{top, grey}$
	$10^{-8}, 1.0$	$10^{-8}, 1.0$	N/A	$10^{-8}, 1.0$
Base pressure	P_{base}	None	None	None
	$P_{top}, 1.0$	N/A	N/A	N/A
Particle size	None	r	r	None
	N/A	$10^{-3}, 10^2$	$10^{-3}, 10^2$	N/A
Shape factor	None	50	Q_0	None
	N/A	Fixed	$0.1, 65$	N/A

slope index, and x is the particle size parameter, given by

$$x = \frac{2\pi r}{\lambda}, \qquad (2)$$

where r is the effective particle radius and λ is the wavelength. The model has four free parameters: κ_0, Q_0, a, and r. The Q_0 parameter is of particular interest because the wavelength at which the extinction efficiency peaks is related to the composition of the aerosol particles, so retrieval of this parameter could provide some constraint on possible cloud species.

The model presented by Kitzmann & Heng (2018) could be extended to include constraints on the vertical location of the cloud; however, here I adopt the version of the model used in F18, which assumes the cloud is spread vertically throughout the atmosphere.

T18 use a special case of this formalism, which fixes Q_0 to 50 and a to 4. They fix κ_0 to 5, but additionally retrieve a cloud mixing ratio χ_c that scales the total opacity in the same way. This model is combined with a simple opaque, grey cloud for pressures $P > P_{top}$.

Finally, Pinhas et al. (2019, hereafter P19) include a cloud model combining an optically thick grey cloud (as used in T18 for $P > P_{top}$) with an overlying haze layer, parametrized by an optical depth scaling and a power-law dependence of extinction with wavelength. This follows on from the model introduced in MacDonald & Madhusudhan (2017):

$$P < P_{top}: \quad \kappa = n_{H_2} a \sigma_0 (\lambda/\lambda_0)^{-\gamma},$$

$$P > P_{top}: \quad \kappa = \infty,$$

where n_{H_2} is the number density of H_2 molecules, σ_0 is the molecular scattering opacity at reference wavelength λ_0, and a here represents the 'Rayleigh enhancement factor' describing the magnitude of additional scattering due to clouds. γ is the dependence of the scattering efficiency on wavelength λ.

All of these four possible parametrizations have been incorporated into the updated version of the NEMESIS spectral retrieval code that works with PYMULTINEST. The free and fixed parameters in each of the models considered, as set in their respective papers, are summarized in Table 1 and Fig. 1. These were incorporated into NEMESIS as far as possible in the same way as in the original papers, but the results have been processed such that they can be compared across models. For example, instead of presenting opacity scaling factors (which differ in meaning between the four models), after the retrieval I combine the relevant parameters from each model to calculate the nadir optical depth at 0.2 μm, and present this value. For the B17 and P19 models, the optical depth is directly equivalent

to the scaling factor due to the fact that the scattering is a simple power law and the cross-section is normalized to 1 at 0.2 μm; for T18 and F18, the scattering cross-section depends on particle size and is not normalized.

The prior ranges for each case, as incorporated into NEMESIS, are also included in Table 1. In general, very wide priors have been used to limit retrieval dependence on the prior, with a few exceptions. The opacity scaling factor range is slightly narrower for T18 and F18 because this does not directly correspond to an optical depth, and keeping the upper end of the range the same as for B17 and P19 resulted in eventual optical depths that were larger than NEMESIS could cope with; however, these ranges are still extremely wide. The other exceptions are for the F18 model, which uses prior ranges for the scattering index and shape factor suggested by the discussion of the model in Kitzmann & Heng (2018). This model is derived from an analytical fit to Mie scattering calculations, and the authors found that typical scattering indices were between 3 and 7, and the shape factor for the various possible species varied from 0.07 to 64.98.

I also test options for all cloud models to incorporate a fractional cloud coverage parameter. This assumes that some fraction f of the terminator has cloud, while the remainder $(1 - f)$ is entirely cloud free. P19 and MacDonald & Madhusudhan (2017) already include a fractional cloud parameter in their analysis; here, I investigate whether the inclusion of an extra free parameter is justified by the information content of current data.

3 RETRIEVAL RESULTS

Here I present and compare the results for each model, for HD 189733b in Section 3.1 and for HD 209458b in Section 3.2. With one exception, all four cloud parametrizations can produce a fit to the data for all scenarios, and the results are generally consistent. I find that there is good evidence in favour of including a terminator cloud fraction parameter for HD 209458b, but a more confused picture for HD 189733b.

A selection of retrievals is shown within the paper, and the full results can be found in an online repository.[1] All corner plots are generated using the CORNER.PY routine (Foreman-Mackey 2016).

Both B17 and P19 found that the H_2O abundances for these hot Jupiters were generally below that expected for a solar composition gas under the conditions of HD 189733b and HD 209458b. The disequilibrium chemistry, solar composition models of Moses et al. (2011) predict $\log(H_2O)$ values of -3.42 and -3.45 for HD 189733 and HD 209458b, respectively. I compare these with the values retrieved in this study below.

3.1 HD 189733b

The spectrum of HD 189733b displays a very steep slope at visible wavelengths, and a muted but still present H_2O feature in the near-infrared. The steep visible slope has generally been attributed to the presence of high-altitude clouds, and the results presented here corroborate this assumption.

The extreme steepness of the visible slope presents a challenge to a completely agnostic approach to retrieval, which aims to place minimal prior constraints on the solution. A very steep slope of this kind can be produced in two ways; either by modelling the cloud such that the extinction efficiency drops off very rapidly with wavelength, or by increasing the temperature and thence the
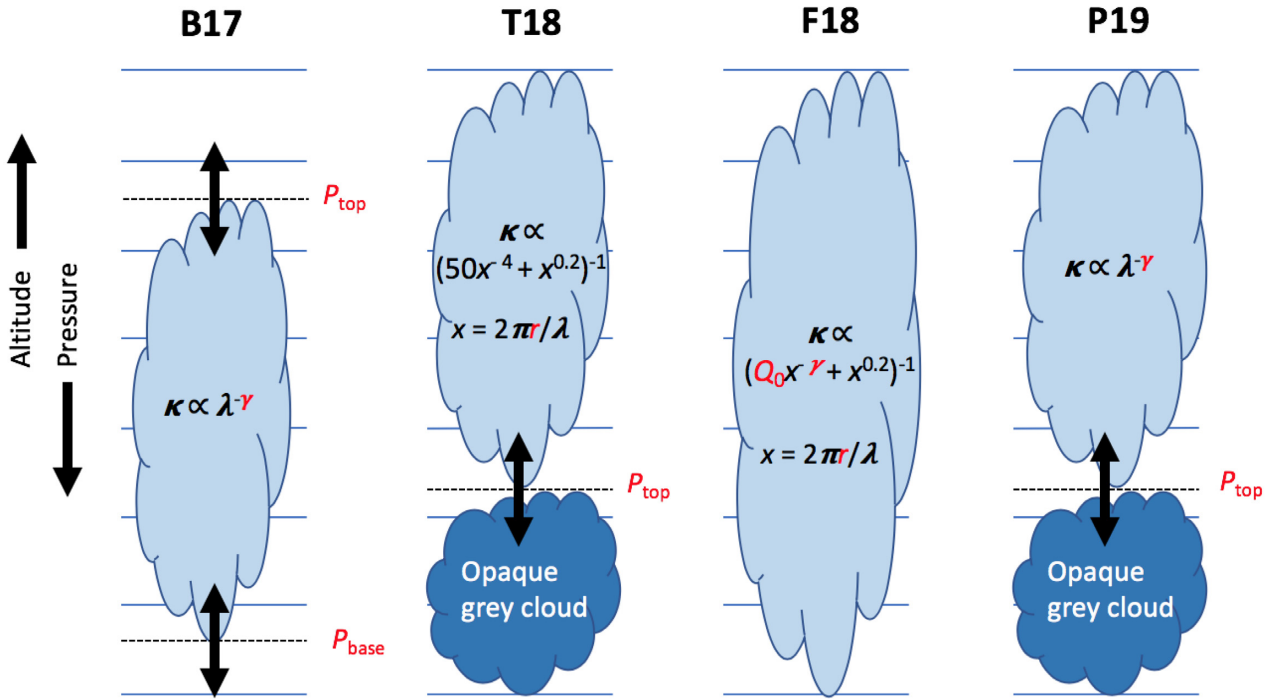
[1] https://tinyurl.com/qvpazxw

Figure 1. A visual indication of how cloud structure is parametrized in each of the models discussed. The parameters highlighted in red are those that are allowed to vary in the retrieval.

scale height of the atmosphere, which increases the amplitude of all features.

For HD 189733b, if the temperature is allowed to vary freely up to a threshold of 3000 K, then the retrieved terminator temperature is around 2000 K for all models. However, we actually have some information about the range of values the terminator temperature can take, since we know the maximum equilibrium temperature of HD 189733b (assuming zero albedo) is around 1200 K (Sing et al. 2016; B17). In transit, for low spectral resolution, the region of the atmosphere that is probed at visible to infrared wavelengths typically covers the range 10^{-4}–0.1 bar (Welbanks & Madhusudhan 2019), which we expect to be broadly isothermal. Therefore, the temperature in the regions of the terminator to which we are sensitive should be $\leq$1200 K, so we can place a (conservative) informative prior on the temperature of 100–1300 K.

I compare the results of the scenarios with and without the informative temperature prior for the B17 and T18 models (Figs 2 and 3). In the case where the retrieved temperature is allowed to exceed the 1300 K limit, the steep visible slope is fit by increasing the scale height via an increase in temperature; for cases where the temperature is restricted, this is compensated for by the scattering index parameter in B17, with the scattering index increasing between the two cases by around 2.75. The T18 model does not allow for a tuneable scattering index, and the result of this is that for the restricted temperature case the T18 model is unable to produce an adequate fit to the data (Fig. 4). This is not a criticism of the T18 study itself, as it dealt only with data from *HST*/WFC3 and the model was not therefore required to simulate a steep optical scattering slope. However, this demonstrates that fixing the values of model parameters should be undertaken with caution.

In the restricted temperature case, temperatures at the high end of the prior range are still favoured. This begs the question as to why the retrieval converges preferentially on solutions involving

high temperatures rather than cases with a steep scattering slope produced by the cloud. I suggest that the reason for this is that the high-temperature solution for the large optical slope relies only on a single model parameter, whereas the solutions involving cloud (regardless of the cloud model chosen) rely on a specific combination of at least three parameters. Occam's razor would therefore favour the temperature solution, and this is only rejected in the light of the prior knowledge we have of the planet's temperature.

I adopt the restricted temperature case as the more plausible scenario, and key retrieved results are shown in Table 2, with spectral fits shown in Fig. 5.

Other points of interest from these results are the consistency of the H_2O abundance results, and the retrieved scattering index, across B17, F18, and P19 for the homogeneous cloud case. All models indicate an H_2O abundance of approximately $1/30\times$ solar, consistent with previous studies B17 and P19, and cloud with a scattering index of around 6.4. Rayleigh scattering corresponds to an index of 4, so the cloud particles present display super-Rayleigh behaviour and are likely to be small. This is discussed further in Section 4.2.

The retrieved cloud top pressures must be compared with more caution, as this parameter represents different things across the four models. In B17 it represents the top of the entire cloud deck, whereas in T18 and P19 it is the top of the grey, opaque cloud. Therefore, the retrieval of a very low top pressure in B17 compared with the others is consistent.

In summary, all models for HD 189733b indicate the presence of small particle cloud high in the atmosphere, and absence of an opaque grey cloud, and subsolar H_2O.

After performing the initial retrievals including homogeneous cloud, I extend the analysis to also include a cloud fraction parameter for all cloud models. Key results from this analysis are presented in Table 2, along with the log of the Bayesian evidence for each
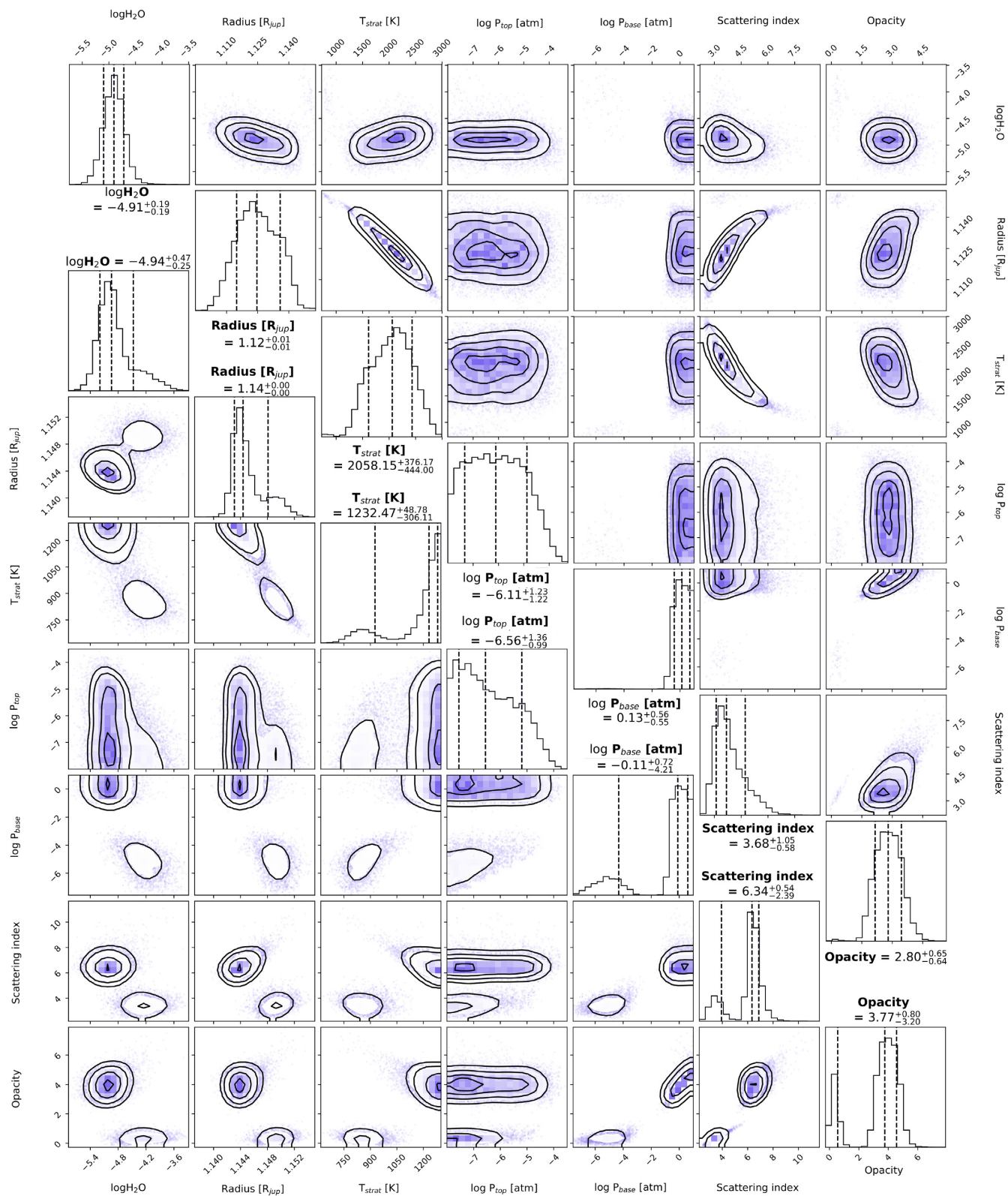
Figure 2. This figure compares posterior corner plots for the B17 cloud model with (bottom left) and without (top right) the informative temperature prior. The secondary solution in the bottom left-hand plot corresponds to the solution presented in B17, arrived at using a more restricted version of the model.

model relative to the model with the highest evidence. This is also known as the Bayes factor. Generally, if the Bayes factor difference is >2, the model with the higher evidence is moderately favoured; if >5 then the higher evidence model is strongly

favoured. It can be seen that the model with the highest evidence for HD 189733b is the P19 model including heterogeneous cloud. The improvement factor for the P19 model when the cloud fraction parameter is added is 6.3, indicating that the heterogeneous cloud
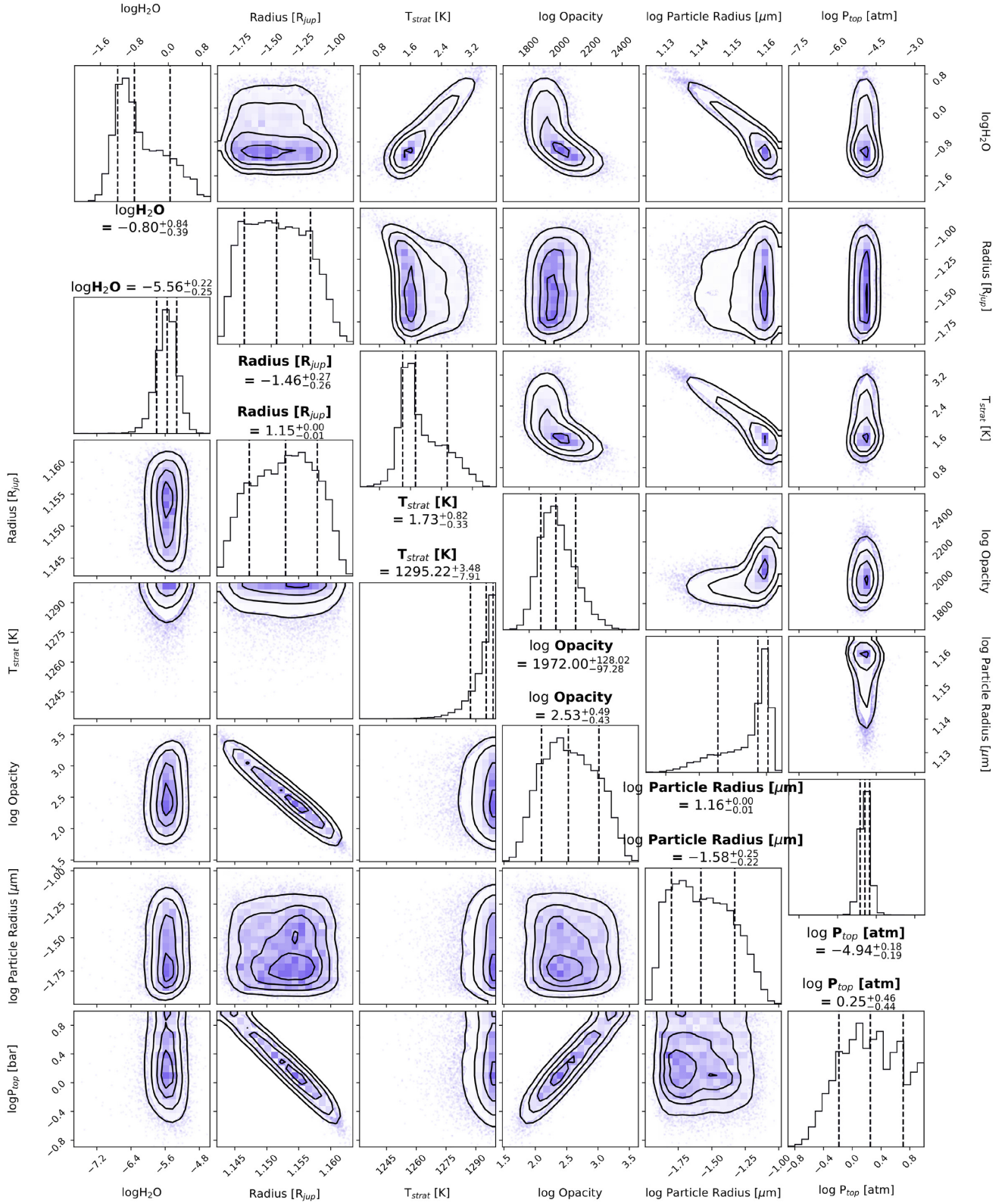
Figure 3. As Fig. 2 but for the T18 model.

is strongly favoured for the P19 model; however, similar improvements when fractional cloud is included are not seen for the other parametrizations, with weak to no evidence for including fractional cloud.

Comparing the different parametrizations against each other, we see that for the fractional cloud case the P19 model significantly outperforms all others. However, if fractional cloud is not included, the B17, F18, and P19 models perform similarly.
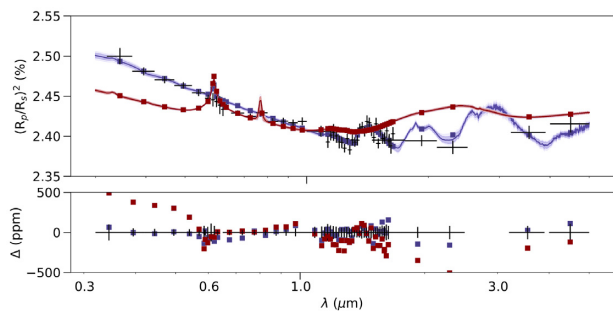
Figure 4. Spectral fits to the HD 189733b data (red) with the T18 model with a restricted temperature prior (dark red) and a broad prior (purple). Spectra are generated using the median values of the posterior distributions. The fit is generally poor for the restricted prior case as the relatively inflexible cloud parametrization does not allow the short wavelength slope to be matched. Shaded regions on the spectrum plot indicate the 2σ envelope for each case.

Table 2. Key retrieval results for HD 189733b. The difference in ln(Bayesian evidence), Δln(BE), is also presented, relative to the best-fitting model of the set. The top row of values for each case is assuming a homogeneous terminator cloud, with the bottom row also retrieving a cloud fraction. The case with the highest Bayesian evidence is highlighted in green. The T18 model is highlighted in red due to the poor quality of the spectral fit.

Property	B17	T18	F18	P19
Log(H$_2$O)	$-4.94^{+0.47}_{-0.25}$	$-5.56^{+0.23}_{-0.25}$	$-5.02^{+0.21}_{-0.21}$	$-4.98^{+0.25}_{-0.23}$
	$-4.72^{+0.32}_{-0.28}$	$-7.50^{+0.39}_{-0.32}$	$-4.94^{+0.25}_{-0.22}$	$-3.58^{+0.50}_{-0.49}$
Scat index	$6.34^{+0.54}_{-2.39}$	N/A	$6.37^{+0.34}_{-0.34}$	$6.47^{+0.52}_{-0.38}$
	$8.13^{+1.44}_{-1.12}$	N/A	$6.62^{+0.26}_{-0.35}$	$10.29^{+1.41}_{-1.12}$
Top pressure	$-6.56^{+1.36}_{-0.99}$	$0.28^{+0.46}_{-0.47}$	N/A	$0.34^{+0.46}_{-0.52}$
	$-7.2^{+0.98}_{-0.55}$	$-3.45^{+2.92}_{-2.99}$	N/A	$-2.29^{+0.74}_{-0.62}$
Cloud fraction	N/A	N/A	N/A	N/A
	$0.68^{+0.17}_{-0.11}$	$0.01^{+0.01}_{-0.01}$	$0.9^{+0.07}_{-0.11}$	$0.61^{+0.07}_{-0.07}$
Δln(BE)	-6.8	-41.9	-6.1	-6.3
	-6.4	-188.9	-8	0

3.2 HD 209458b

Model fits to HD 209458b proved more straightforward than for HD 189733b due to the lack of a substantial scattering slope in the optical part of the spectrum (fits are shown in Fig. 6). The retrieved temperature is in the range expected for the planet, even when a less restrictive temperature prior is used. The T18 model is also able to produce a good fit to the data in this case.

The key results for HD 209458b are presented in Table 3. As for HD 189733b, the best-fitting model is highlighted in green, and tests are run for both homogeneous and heterogeneous cloud.

Again, the retrieved H$_2$O abundance is consistently subsolar across all models tested, at around 10 parts per million volume (ppmv). Unlike the HD 189733b case, however, the evidence is more strongly in favour of a grey cloud deck, as both T18 and P19 models have top pressures that would make the grey cloud deck visible (see e.g. Fig. 7). By contrast, the top pressure of the B17 model is higher than for HD 189733b, indicating that the upper part of the atmosphere is more likely to be cloud free.

All four models agree well on cloud fraction for the heterogeneous cloud case, and all four also show a substantial improvement in the goodness of fit when the cloud fraction parameter is included, with Bayesian evidence indicating that fractional cloud is strongly
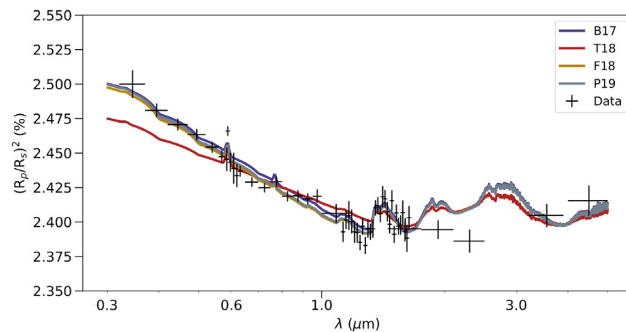

Figure 5. Spectral fits to the HD 189733b data for all models, for the restricted temperature case without fractional cloud. The model spectra are calculated using the median parameter values.
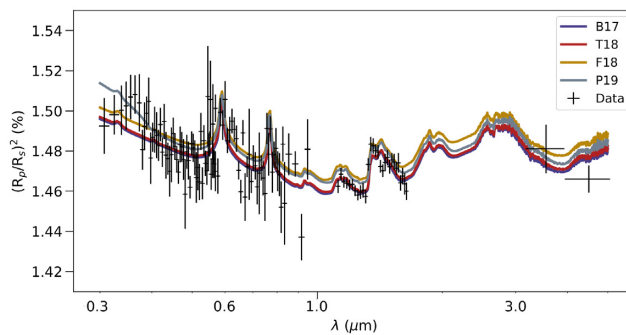

Figure 6. As Fig. 5 but for HD 209458b, for models including a fractional cloud parameter.

Table 3. Key retrieval results for HD 209458b, as Table 2.

Property	B17	T18	F18	P19
Log(H$_2$O)	$-4.89^{+0.23}_{-0.23}$	$-5.02^{+0.17}_{-0.15}$	$-5.11^{+0.16}_{-0.15}$	$-4.95^{+0.24}_{-0.19}$
	$-5.15^{+0.12}_{-0.11}$	$-5.19^{+0.14}_{-0.14}$	$-5.18^{+0.13}_{-0.12}$	$-5.06^{+0.17}_{-0.17}$
Scat index	$3.69^{+5.16}_{-2.64}$	N/A	$5.08^{+1.31}_{-1.36}$	$8.79^{+3.49}_{-5.33}$
	$3.12^{+2.48}_{-1.95}$	N/A	$4.84^{+1.33}_{-1.17}$	$8.23^{+3.62}_{-4.07}$
Top pressure	$-0.65^{+0.26}_{-2.95}$	$-0.79^{+0.37}_{-0.13}$	N/A	$-0.61^{+0.16}_{-0.11}$
	$-2.89^{+0.81}_{-1.05}$	$-3.64^{+3.01}_{-2.88}$	N/A	$-5.6^{+2.14}_{-1.6}$
Cloud fraction	N/A	N/A	N/A	N/A
	$0.37^{+0.05}_{-0.05}$	$0.44^{+0.07}_{-0.08}$	$0.33^{+0.06}_{-0.05}$	$0.39^{+0.06}_{-0.08}$
Δln(BE)	-10.9	-9.4	-7.3	-9
	-5.3	-1.3	-4	0

favoured. With fractional cloud included, the cloud top pressure for the T18 and P19 models is reduced (compare e.g. Fig. 8 with Fig. 7), as partial cloud high up has a similar observational signature to opaque cloud lower down.

F18 (Fig. 9) and P19 have higher scattering indices than B17, but in the case of P19 there is relatively low opacity for the upper cloud/haze above the opaque grey cloud, as in this case the grey cloud dominates the signal.

For the case where fractional cloud is included, the T18 and P19 models have similar evidence, whereas B17 and F18 are strongly and moderately disfavoured with respect to P19. T18 and P19 both include an opaque cloud deck, reinforcing the fact that HD 209458b is likely to have grey cloud.
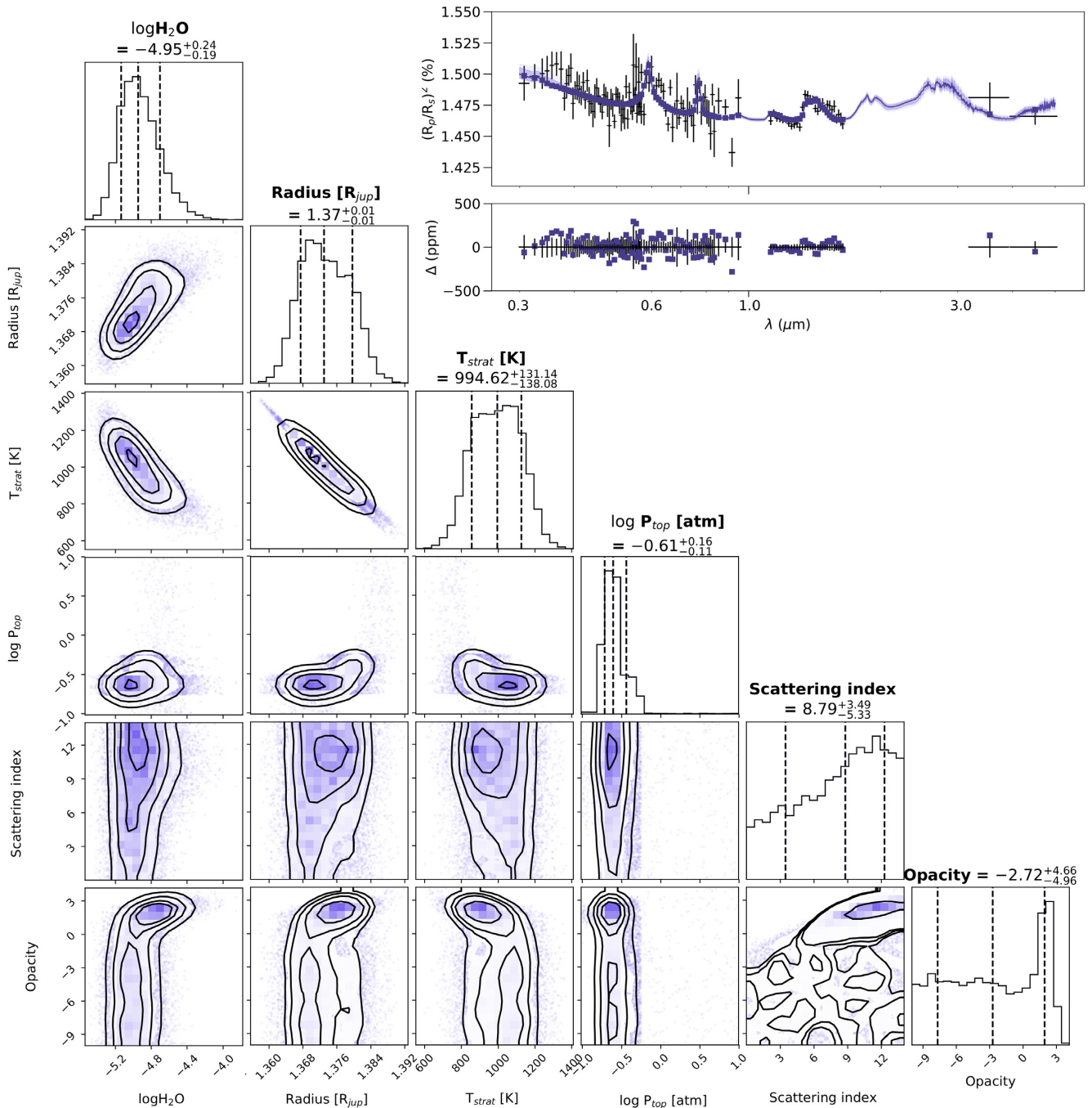
Figure 7. Posterior probability distributions (excluding alkali metals) and best-fitting spectrum for HD 209458b using the P19 cloud model with 100 per cent terminator cloud cover. The spectrum is generated using the median values of the posterior distributions. Shaded regions on the spectrum plot indicate the 1σ (darker) and 2σ (paler) envelopes.

4 DISCUSSION

Despite the fact that the four models include different ways of parametrizing the cloud, for the most part a coherent picture emerges. These are visually summarized for each planet in Fig. 10.

For both cases, the P19 model emerges as the one that provides the best fit to the observed spectra. The combination of grey cloud and overlying haze with a tunable scattering index seems to provide the most flexibility.

Below, I discuss the major findings about H_2O abundance, cloud scattering properties, and cloud location for each planet. I contrast the

findings with those presented in the P19 paper. A similar comparison for the results from F18 and T18 is not relevant, as these two papers dealt with only a limited subset of the data considered here.

4.1 H_2O abundance

For both planets, the retrieved H_2O abundance is generally very robust to different assumptions about cloud, echoing similar findings by Mai & Line (2019). The exception to this is the heterogeneous cloud P19 model for HD 189733b, which has a retrieved $\log(H_2O)$
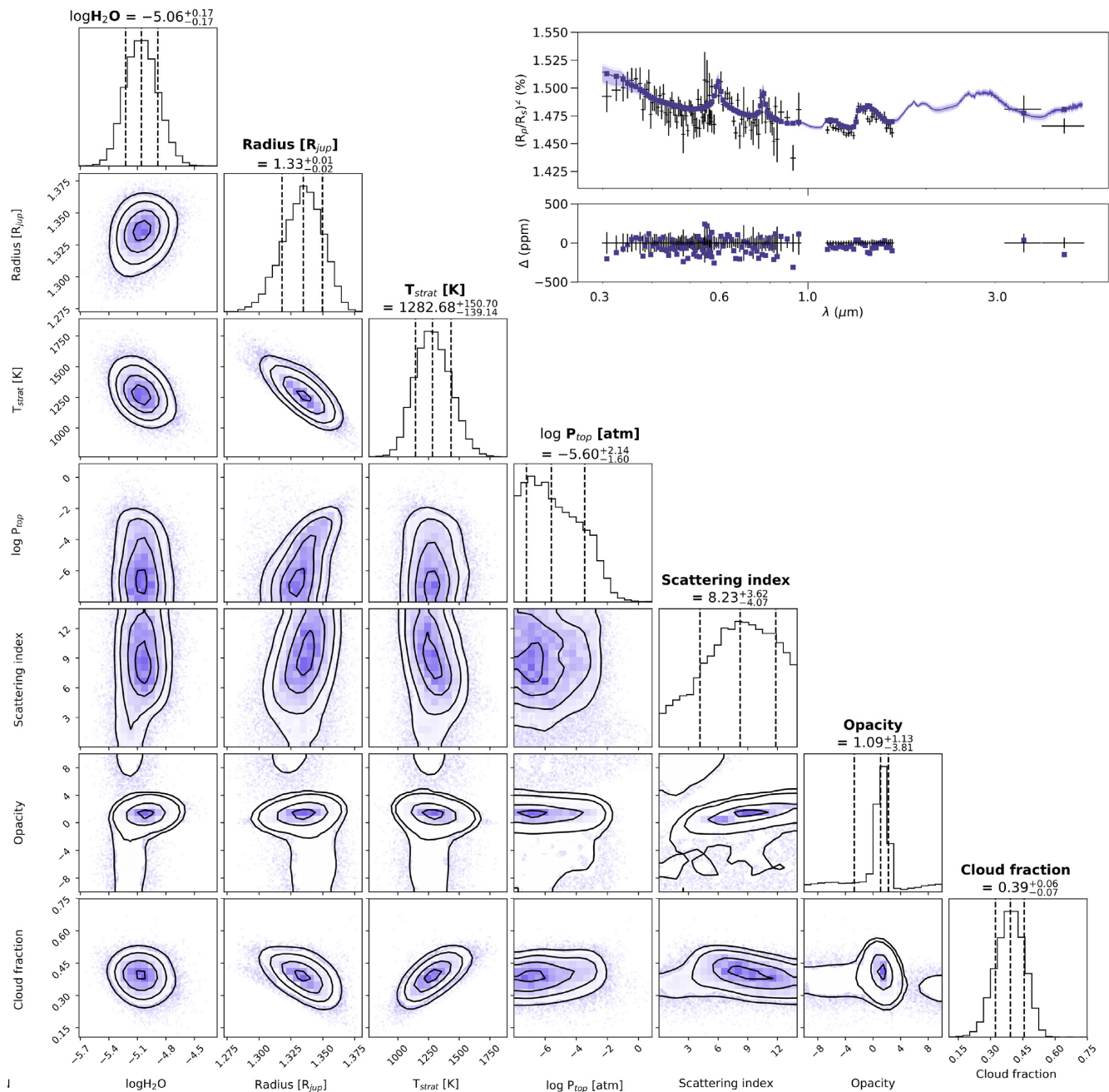
Figure 8. As Fig. 7 but including a fractional cloud parameter.

abundance of -3.58, meaning the H_2O volume mixing ratio is an order of magnitude higher than for all other models. This is also substantially higher than the retrieved value from the P19 paper itself (-5.04). The trade-off that causes this can be traced to differences in the retrieved cloud properties between the homogeneous model in this study, the results of P19 and the heterogeneous case here. The P19 study has a retrieved scattering index of ~ 8, compared with 6.47 for the P19 parametrization in this work for the homogeneous case and 10.29 for the heterogeneous case. The higher the scattering index, the more rapidly the haze extinction efficiency drops off as a function of wavelength. To compensate for the lack of cloud opacity at longer wavelengths when the scattering index is high, the grey cloud top pressure for the heterogeneous P19 model in this work is reduced to -2.29 from 0.34 in the homogeneous

model. The grey cloud moving higher up means that a higher H_2O abundance is required to fit the 1.4 μm feature in the WFC3 bandpass.

Another key difference between this work and P19 is that this work also includes the bandpass integrated points from the *HST*/Near Infrared Camera and Multi-Object Spectrometer (NICMOS) instrument, as published by Pont et al. (2013) after Gibson et al. (2012). P19 did not include these points, and if they are removed and the fits using the P19 model are repeated, the solution is closer to the P19 published result, especially given the large error bars on the H_2O abundance (Table 4).[2]

---

[2]The fractional cloud case without NICMOS points for the P19 model has bimodal probability distributions for the radius and cloud top pressures
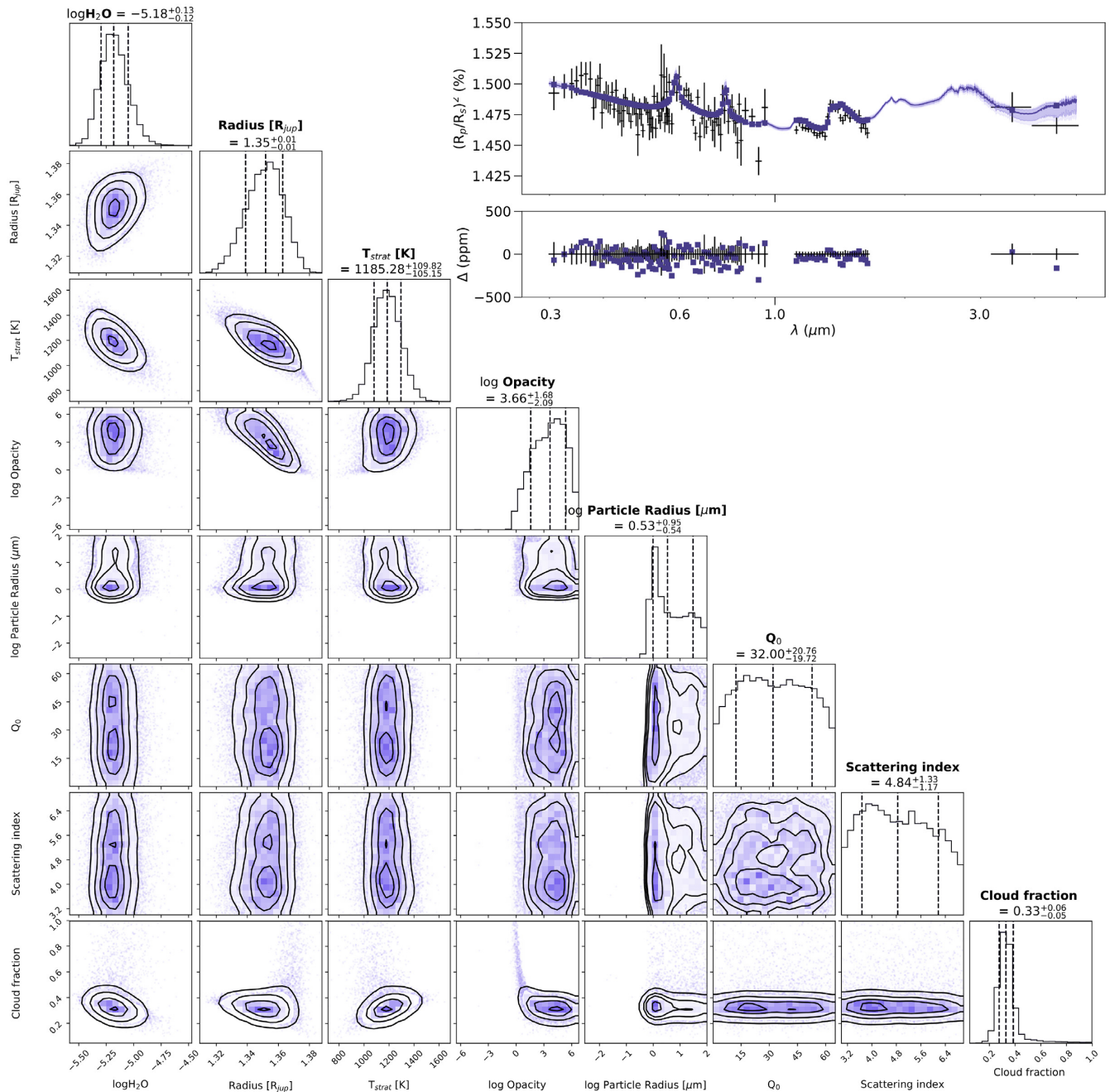
Figure 9. Posterior probability distributions (excluding alkali metals) and best-fitting spectrum for HD 209458b using the F18 cloud model with fractional terminator cloud cover. The spectrum is generated using the median values of the posterior distributions. Shaded regions on the spectrum plot indicate the 1σ (darker) and 2σ (paler) envelopes.

All H_2O abundance values for HD 209458b are consistent within 1σ for homogeneous and heterogeneous cloud models, and within 2σ between homogeneous and heterogeneous models. The H_2O abundance is also consistently subsolar, as for HD 189733b, compared with the value predicted by Moses et al. (2011) of -3.45. The retrieved H_2O abundance from the P19 paper is $-4.66^{+0.39}_{-0.30}$, slightly

higher than the values presented here, but the probability distributions overlap at the 1σ level.

A likely explanation for any remaining differences between this work and the P19 paper is our different approaches to temperature profile parametrization. In this work, I use a simple model assuming an isotherm plus an adiabat, whereas the more complex six-parameter model of P19 allows greater freedom in the structure of the T–p profile. Whilst in the region of greatest sensitivity the T–p profiles are consistent with each other, variation in the lower atmosphere (where there is little constraint) could alter the deep atmosphere scale height, which could in turn affect the other retrieved properties.
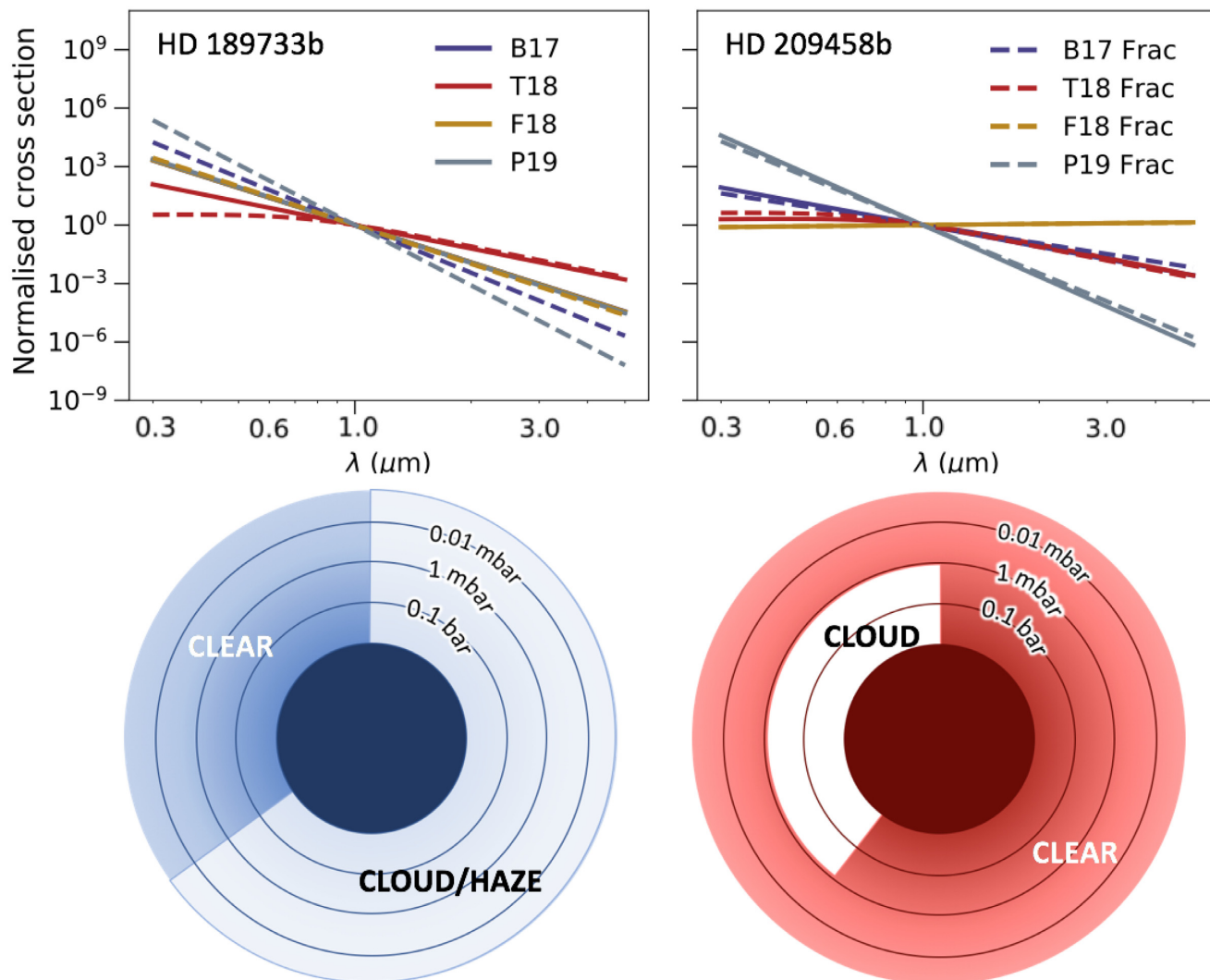
(figures in online material). The result of this is that the spectrum generated using the median values actually does not provide a good fit, as the median falls in between the probability maxima. The maximum likelihood solution produces a spectrum that provides a much better fit to the observation.

Figure 10. A visual summary of the retrieved cloud structure and scattering behaviour. The cloud structure as shown emerges from the combined information of all four models, which indicates that HD 189733b has small-particle aerosols that cover at least 60 per cent of the terminator, reaching to low pressures, but no grey cloud; and HD 209458b has opaque grey cloud deep in the atmosphere covering around 40 per cent of the terminator. The top panels show the wavelength dependence of the cloud extinction cross-section for each model case. The cross-sections are normalized to the values at 1 μm for comparison. The solid lines indicate the result for homogeneous cloud and the dotted lines for fractional cloud cover.

Table 4. Comparison of retrieved results without the HD 189733b NICMOS data points from this work and P19. Error bars are not quoted for P19 values where they are not specified in detail in the paper. Values without error bars are as read from probability distribution histograms.

Property	100% cloud	Fractional cloud	P19
Log(H$_2$O)	$-5.21^{+0.21}_{-0.21}$	$-4.23^{+0.79}_{-0.72}$	$-5.04^{+0.46}_{-0.30}$
Scat index	$6.49^{+0.48}_{-0.37}$	$10.52^{+1.79}_{-1.84}$	7.75
Top pressure	$0.45^{+0.37}_{-0.38}$	$-1.36^{+1.72}_{-1.22}$	0.4
Cloud fraction	N/A	$0.58^{+0.11}_{-0.08}$	0.67

4.2 Scattering properties

Pinhas & Madhusudhan (2017) investigate the most representative scattering slope index for a range of possible cloud compositions with different particle sizes, and find that values of around 6 can be achieved with modal sizes of 0.01 μm for Na$_2$S and ZnS, and 0.1 μm for MnS. These slopes are only relevant across relatively narrow

spectral ranges in the optical, and a full study of the effective cross-sections for these species in Pinhas & Madhusudhan (2017) shows that the curve somewhat flattens out in the near-infrared. In reality, the variation of extinction cross-section as a function of wavelength is much more complex than a simple power-law relationship.

However, it is clear that an extremely steep scattering slope is required to fit the optical spectrum for HD 189733b that extends throughout the optical region. This slope does not appear to be achievable within any single species tested by Pinhas & Madhusudhan (2017). A secondary solution, indicated by the homogeneous B17 model (see Fig. 2), is that a steep slope is created by a detached haze layer high in the atmosphere that becomes optically thin at longer wavelengths. Other more complex solutions could include layered clouds of different species.

Previous explanations for the steep slope have also included unocculted starspots (McCullough et al. 2014), although the data used in this work were in fact already corrected for unocculted starspots according to the method outlined by Pont et al. (2013).

However, this method was only able to account for the variable level of starspots, whilst the baseline spot coverage remains unknown and could still have an effect (Rackham, Apai & Giampapa 2018).

Our best hope for further understanding the cloud properties of HD 189733b is that *JWST* will uncover spectral signatures of a specific condensate in the infrared (e.g. Wakeford & Sing 2015); at this point, it is unclear which effect of many is responsible for the steep optical slope.

No such explanations need to be invoked for HD 209458b, as relatively flat spectra like this can be produced by any condensate with a large spread of particle sizes. Whilst retrieved scattering indices are high for the P19 model, this refers only to the upper layer of cloud that has a low optical depth – it is the grey cloud deck for this and for the T18 model that provides the majority of the cloud opacity. The scattering index for B17 and F18 is much lower for HD 209458b than for HD 189733b. I therefore conclude that the cloud on HD 209458b is consistent with cloud containing large aerosol particles.

4.3 Location of cloud

Again, the picture is more complicated for HD 189733b than for HD 209458b. Whilst all cases are consistent with a low top pressure for a small particle haze (from the B17 model), and a relatively high top pressure for any grey cloud that might be present (from T18 and P19), there is ambiguity about the spatial location of the cloud. Whilst with the best-fitting P19 model there is a clear improvement when a fractional cloud parameter is included, this is not the case for the B17 or F18 models.

The retrieved cloud fraction from the P19 model is consistent with the value from the P19 paper itself, although the probability distribution from the P19 paper is double peaked and also has a secondary maximum close to 1.0. This reflects the spread of cloud fraction values from the other models tested in this work. There is also substantial degeneracy between the grey cloud top pressure and cloud fraction for the P19 model, as when a fractional cloud parameter is included the top pressure decreases from greater than 1 bar[3] to less than 10 mbar (Table 2). The lower value here is not consistent with the result from P19 that has the grey cloud top pressure at around 1 bar, but removing the NICMOS points reduces the retrieved pressure in this work to a somewhat closer value (Table 4). In any event, the degeneracy first pointed out in Line & Parmentier (2016) between global and patchy cloud is evident here.

On the other hand, there is strong and consistent evidence that HD 209458b has a terminator with only ∼40 per cent cloud coverage. This is also in reasonable agreement with the value from the P19 paper, which has a cloud fraction of 51 per cent, with the probability distribution overlapping with the one in this work.

The location of the cloud top for HD 209458b is a little more ambiguous than for HD 189733b, because once again there is substantial degeneracy between the cloud fraction and the cloud top pressure. Lower cloud top pressures are permitted for fractional terminator cloud coverage, as their relative effects on the cloud opacity cancel out. Indeed, for the P19 model the top of the grey cloud deck could be very high in the atmosphere, which may be somewhat implausible as large particles would be unlikely to be lofted to pressures of order a few μbar. However, it should be noted

that the constraint for the P19 model is only an upper limit on the cloud top pressure.

HD 189733b and HD 209458b have fairly similar equilibrium temperatures; HD 209458b is around 300 K warmer. They key difference relevant here is probably that HD 209458b is a highly inflated planet, whereas HD 189733b has a relatively high gravity for a hot Jupiter. This might explain why the cloud on HD 189733b appears to be composed of much smaller particles than on HD 209458b, as large particles would be more likely to rain out in a higher gravity environment.

Assuming that the cloud on HD 189733b and HD 209458b may be made of the same substance, the presence of cloud at only part of the terminator on HD 209458b may be due to its higher equilibrium temperature. Whilst the temperature may be suitable for cloud on both terminators for HD 189733b, the dayside and evening terminator of HD 209458b may be too warm for cloud to persist.

4.4 Alkali metals

In this paper, I have focused on the retrievals of H_2O abundance and cloud properties rather than the alkali metals. Na is detected in both atmospheres, whilst only an upper limit for K can be obtained for HD 189733b. In general, the retrieved abundances are consistent between cloud models, although the presence of fractional cloud affects the Na abundance for HD 189733b.

For HD 189733b (without fractional cloud), Na and K abundances are approximately 600 and 0.03 ppmv, respectively; when fractional cloud is included, the Na abundance is reduced to ∼10 ppm. For HD 209458b, Na and K abundances are approximately 200 and 4 ppmv. Whilst the K abundances are reasonably aligned with expectations (solar abundance from Asplund et al. 2009 is ∼0.1 ppmv), the Na abundances are surprisingly high (several hundred ppmv, as opposed to ∼2 ppmv from Asplund et al. 2009). The full Na and K retrieved results are included in the online repository that accompanies this paper.

As mentioned in B17, the limited resolution of the K tables in the model presents a challenge when fitting the centre of the alkali metal absorption bands, since these are observed using narrower wavelength bins than the rest of the spectrum. This is likely to be a factor in the somewhat unrealistic Na abundances from the retrieval, and means that the retrieved abundances should not be relied on. This is unlikely to affect other retrieved properties, since the continuum in both spectra is dominated by cloud rather than by the alkali line wings.

5 CONCLUSIONS

This paper has explored a range of cloud parametrizations that exist in the literature and applied them to spectra of HD 189733b and HD 209458b. I find that, whilst each model has different approaches to representing cloud, the retrieval results taken together present a surprisingly coherent and holistic picture of each planet. HD 189733b most likely has cloud made of small particles spread throughout the region of the atmosphere to which we are sensitive, whereas HD 209458b displays a thicker cloud with larger particles that is restricted both to lower regions of the atmosphere and to roughly 40 per cent of the terminator. Both planets have H_2O abundances that are consistently retrieved to be subsolar, confirming the previous findings of B17 and P19.

Despite their relatively similar equilibrium temperatures, and apparently similar chemistry extrapolated from their H_2O abundances, the cloud properties of the two planets indicate very different regimes.

---

[3]NEMESIS uses units of atmospheres for pressure. 1 atm = 1.01325 bar.

The lack of large particles on HD 189733b may be attributable to its higher gravity, whereas in the partially cloudy terminator on HD 209458b we may be seeing the effect of a slightly warmer eastern (evening) terminator.

We now have access to an ever increasing number of hot Jupiters with spectra covering the optical and infrared, so this type of analysis can and should be expanded to cover a broader range of targets. The *JWST* will provide more insight by probing further into the infrared, and could potentially reveal what these mysterious clouds are made of.

DATA AVAILABILITY

The data for HD 189733b and HD 209458b used in this paper are as published by Sing et al. (2016). The spectra are available to download here:

https://pages.jh.edu/~dsing3/spectra/HD189733b_Sing_2015_Nature.csv

https://pages.jh.edu/~dsing3/spectra/HD209458b_Sing_2015_Nature.csv

REFERENCES

Asplund M., Grevesse N., Sauval A. J., Scott P., 2009, ARA&A, 47, 481
Barber R. J., Tennyson J., Harris G. J., Tolchenov R. N., 2006, MNRAS, 368, 1087
Barstow J. K., Heng K., 2020, Space Sci. Rev., 216, 82
Barstow J. K., Aigrain S., Irwin P. G. J., Sing D. K., 2017, ApJ, 834, 50 (B17)
Benneke B., 2015, preprint (arXiv:1504.07655)
Blecic J., Dobbs-Dixon I., Greene T., 2017, ApJ, 848, 127
Borysow A., 2002, A&A, 390, 779
Borysow A., Frommhold L., 1989, ApJ, 341, 549
Borysow A., Frommhold L., 1990, ApJ, 348, L41
Borysow A., Frommhold L., Moraldi M., 1989, ApJ, 336, 495
Borysow A., Jorgensen U. G., Fu Y., 2001, J. Quant. Spectrosc. Radiat. Transf., 68, 235
Bouchy F. et al., 2005, A&A, 444, L15
Buchner J. et al., 2014, A&A, 564, A125
Charbonneau D., Brown T. M., Latham D. W., Mayor M., 2000, ApJ, 529, L45
Cubillos P. E. et al., 2017, ApJ, 849, 145
Feroz F., Hobson M. P., 2008, MNRAS, 384, 449
Feroz F., Hobson M. P., Bridges M., 2009, MNRAS, 398, 1601
Feroz F., Hobson M. P., Cameron E., Pettitt A. N., 2019, Open J. Astrophys., 2, 10
Fisher C., Heng K., 2018, MNRAS, 481, 4698 (F18)
Foreman-Mackey D., 2016, J. Open Source Software, 1, 24
Gibson N. P., Aigrain S., Roberts S., Evans T. M., Osborne M., Pont F., 2012, MNRAS, 419, 2683
Heiter U. et al., 2008, J. Phys.: Conf. Ser., 130, 012011
Helling C. et al., 2016, MNRAS, 460, 855
Hörst S. M., 2017, J. Geophys. Res.: Planets, 122, 432
Irwin P. G. J. et al., 2008, J. Quant. Spectrosc. Radiat. Transf., 109, 1136
Kitzmann D., Heng K., 2018, MNRAS, 475, 94
Kitzmann D., Heng K., Oreshenko M., Grimm S. L., Apai D., Bowler B. P., Burgasser A. J., Marley M. S., 2020, ApJ, 890, 174
Krissansen-Totton J., Garland R., Irwin P., Catling D. C., 2018, AJ, 156, 114
Lacis A. A., Oinas V., 1991, J. Geophys. Res., 96, 9027
Lavie B. et al., 2017, AJ, 154, 91
Lee J.-M., Fletcher L. N., Irwin P. G. J., 2012, MNRAS, 420, 170
Lee J.-M., Heng K., Irwin P. G. J., 2013, ApJ, 778, 97
Line M. R., Parmentier V., 2016, ApJ, 820, 78
Line M. R. et al., 2013, ApJ, 775, 137
McCullough P. R., Crouzet N., Deming D., Madhusudhan N., 2014, ApJ, 791, 55
MacDonald R. J., Madhusudhan N., 2017, MNRAS, 469, 1979
Madhusudhan N., Seager S., 2009, ApJ, 707, 24
Mai C., Line M. R., 2019, ApJ, 883, 144
Mollière P. et al., 2020, A&A, preprint (arXiv:2006.09394)
Moses J. I. et al., 2011, ApJ, 737, 15
Pinhas A., Madhusudhan N., 2017, MNRAS, 471, 4355
Pinhas A., Madhusudhan N., Gandhi S., MacDonald R., 2019, MNRAS, 482, 1485 (P19)
Pont F., Sing D. K., Gibson N. P., Aigrain S., Henry G., Husnoo N., 2013, MNRAS, 432, 2917
Rackham B. V., Apai D., Giampapa M. S., 2018, ApJ, 853, 122
Rodgers C. D., 2000, Inverse Methods for Atmospheric Sounding: Theory and Practice. World Scientific Press, Singapore
Sing D. K. et al., 2016, Nature, 529, 59
Tsiaras A. et al., 2018, AJ, 155, 156 (T18)
Wakeford H. R., Sing D. K., 2015, A&A, 573, A122
Wakeford H. R., Visscher C., Lewis N. K., Kataria T., Marley M. S., Fortney J. J., Mandell A. M., 2017, MNRAS, 464, 4247
Waldmann I. P., Tinetti G., Rocchetto M., Barton E. J., Yurchenko S. N., Tennyson J., 2015, ApJ, 802, 107
Welbanks L., Madhusudhan N., 2019, AJ, 157, 206
Welbanks L., Madhusudhan N., Allard N. F., Hubeny I., Spiegelman F., Leininger T., 2019, ApJ, 887, L20

This paper has been typeset from a TEX/LATEX file prepared by the author.